npj | 2D materials and applications

www.nature.com/npj2dmaterials

ARTICLE OPEN

Check for updates

Electronic transport in graphene with out-of-plane disorder

Yifei Guan[1] and Oleg V. Yazyev[1]✉

Real-world samples of graphene often exhibit various types of out-of-plane disorder–ripples, wrinkles and folds–introduced at the stage of growth and transfer processes. These complex out-of-plane defects resulting from the interplay between self-adhesion of graphene and its bending rigidity inevitably lead to the scattering of charge carriers thus affecting the electronic transport properties of graphene. We address the ballistic charge-carrier transmission across the models of out-of-plane defects using tight-binding and density functional calculations while fully taking into account lattice relaxation effects. The observed transmission oscillations in commensurate graphene wrinkles are attributed to the interference between intra- and interlayer transport channels, while the incommensurate wrinkles show vanishing backscattering and retain the transport properties of flat graphene. The suppression of backscattering reveals the crucial role of lattice commensuration in the electronic transmission. Our results provide guidelines to controlling the transport properties of graphene in presence of this ubiquitous type of disorder.

npj 2D Materials and Applications (2024)8:1 ; https://doi.org/10.1038/s41699-023-00437-6

INTRODUCTION

Being the first and the most investigated two-dimensional (2D) material, graphene continues attracting attention as a platform for exploring novel physics and realizing prospective technological applications[1,2]. The 2D nature of graphene gives rise to soft flexural modes that result in low-energy out-of-plane disorder otherwise absent in bulk, three-dimensional materials[3–6]. The interplay between bending upon in-plane compression and the interlayer adhesion results in several distinct types of out-of-plane disorder: ripples, wrinkles and folds (see refs. [3,7] and Fig. 1a, b). The out-of-plane disorder has a prominent effect on the electronic structure and transport properties of graphene[8–11]. Finite curvature of the deformed region results in pseudo-gauge fields[12,13], while the collapsed regions in wrinkles and folds provide a pathway for electronic tunnelling between layers[7,14]. In addition, out-of-plane disorder locally accumulates charges and acts as scattering centers[7,15–17], subsequently having an impact on the operation of graphene-based nanoscale electronic devices[14,18,19] as well as electrical characteristics of large-scale graphene samples.

Out-of-plane disorder in graphene may occur for several reasons. For instance, graphene grown using the chemical vapour decomposition (CVD) process develops wrinkles and folds as a result of the thermal contraction of substrate during the cooling stage[20–22]. The out-of-plane disorder may also be introduced during the transfer procedure[23,24]. Significant efforts have then be devoted to eliminating wrinkles[3,21], e.g. by using the substrates with matching thermal expansion coefficients[23], strain engineering[25] and tailored temperature control protocols[21]. Experimental studies of the electronic transport in graphene with out-of-plane disorder have also been published[7,26]. It was proposed that controlled folding of graphene can be used for engineering charge-carrier dynamics[27–30]. No question, future applications of graphene in electronics call for a detailed understanding of the effect of this ubiquitous type of disorder on the electronic transport.

In this work, we systematically investigate the electronic transport across wrinkles and folds in graphene using first-principle computations. For commensurate graphene wrinkles, in which the interlayer stacking corresponds to the energetically favorable Bernal stacking configuration, we find that the electronic transmission oscillates over wide energy ranges. The observed oscillation patterns are attributed to quantum interference between the inter- and intralayer transport channels. In incommensurate wrinkles and folds, the mismatch between the layers is found to suppresses the interlayer tunneling resulting in transmission probabilities close to the limit of flat, pristine graphene.

RESULTS

Construction of models

The atomistic models of graphene with out-of-plane disorder considered in our work are defined by a compressive displacement of length Δ_W (see Fig. 1a) forming a wrinkle or a fold along crystallographic vector $\mathbf{v} = (a, b)$. The considered configurations are thus assumed to be periodic along $\mathbf{v}$. The interplay between the bending energy and attractive interlayer interactions of graphene layers define the evolution across the three types of out-of-plane disorder realized upon increasing Δ_W as shown in Fig. 1b. While ripples are formed at small Δ_W, interlayer attraction collapses such structures to wrinkles for larger values of Δ_W, and further increase of Δ_W leads to folds, in which the contact area between graphene layers is further increased. Extremities of wrinkles and folds have loop-like structures free of interlayer coupling[7]. In our work, we focus on the latter two types of out-of-plane defects since it is the interlayer coupling between graphene layers that is expected to have strong effects on the electronic transport. All atomistic models of wrinkles and folds considered in our work have been constructed with the help of classical force-field relaxation (see the Methods section for details).

Electronic transport across commensurate wrinkles

We first consider the special case of wrinkles defined by $\mathbf{v} = (1, 0)$ and $\mathbf{v} = (1, 1)$, referring to them as zigzag and armchair, respectively. The collapsed regions of such wrinkles are compatible with the energetically favorable Bernal interlayer stacking configuration[31–34], and hence referred to as commensurate in the rest of our paper. For these relaxed models, we calculated ballistic charge-carrier transmission from first principles, using the combination of density functional theory (DFT) and the non-equilibrium Green's function

[1]Institute of Physics, École Polytechnique Fédérale de Lausanne (EPFL), CH-1015 Lausanne, Switzerland. ✉email: oleg.yazyev@epfl.ch

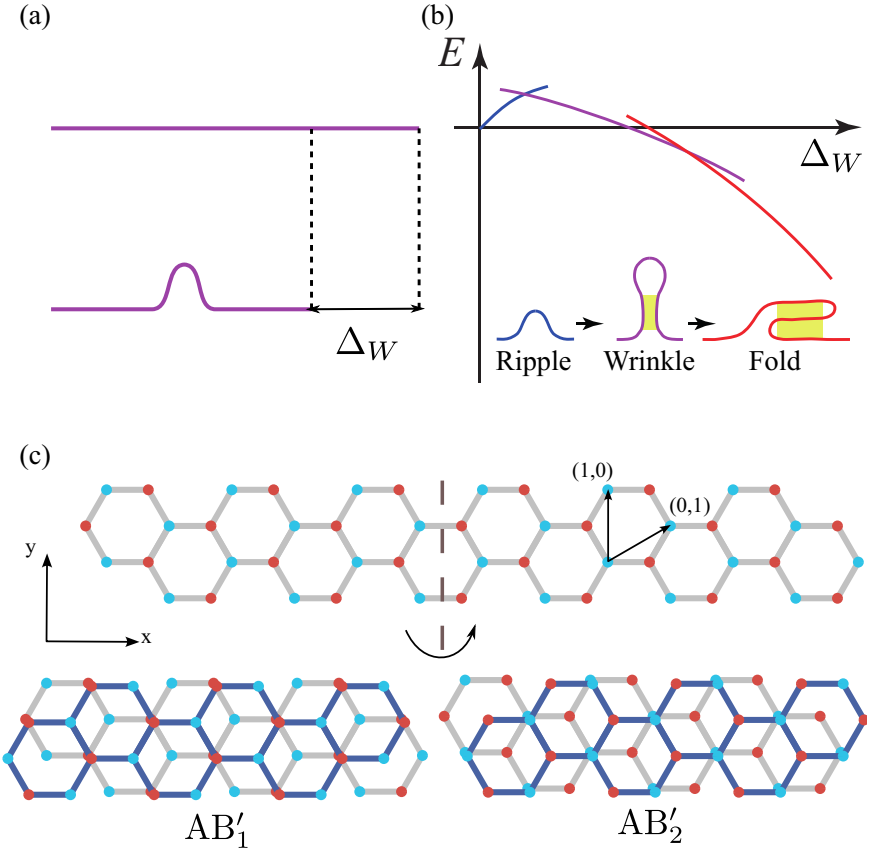

Fig. 1 The structure of out-of-plane disorder in graphene. a Definition of compressive displacement Δ_W relative to the flat, unstrained graphene. **b** Formation of the three distinct types of out-of-plane disorder upon increasing Δ_W. The curves show a schematic illustration of the dependence of energy E on Δ_W for the three deformation regimes. Yellow color exposes the collapsed regions where the interlayer coupling is enabled. **c** Illustration of the interlayer coupling between the atoms belonging to the same sublattice in commensurate zigzag wrinkles and folds.

formalism implemented in the TranSIESTA package[35,36] (see Methods). The results of DFT calculations are discussed in comparison with the tight-binding (TB) approximation calculations employing the Slater-Koster formalism[7,37] (see the Supplementary Information document as well as the Methods section for the details on methodology). Figure 2a–d present the ballistic transmission $T(E, k_{//})$ for the models of zigzag wrinkles defined by $\Delta_W = 40$, 60, 120 and 240 Å as a function of energy E and momentum parallel to the wrinkle $k_{//}$. Furthermore, each panel shows transmission $T(E)$ plotted at a specific $k_{//} = \pm 2\pi/(3a_0)$ ($a_0 = 2.46$ Å is the lattice constant of graphene), which corresponds to the momentum of projections of the Dirac cone band degeneracies. The ballistic transmissions $T(E, k_{//})$ describes single scattering events on periodic wrinkles or folds. Converting these result into measurable values of conductance requires the knowledge of the device width W. Conductance per transmission channel $G(k_{//}, E)$ is given by $G(k_{//}, E) = T(k_{//}, E)G_0$, where the conductance quantum $G_0 = 2e^2/h = 7.748 \times 10^{-5}$ S, including spin degeneracy. The total conductance $G(E)$ is given by a summation over momenta $k_{//}$ permitted by the Born-von Karman boundary conditions: $G(E) = \sum_i G_0 T(k_i, E)$, with $k_i = i \cdot 2\pi/(W/a)$. This conductance corresponds to charge-carrier energy E and is calculated in the zero-bias limit.

There are two striking observations in the presented transmission plots. Firstly, both in DFT and TB results, we observe a pronounced electron-hole asymmetry in the charge-carrier transmission. The electron-hole asymmetry has an origin in the interlayer stacking of zigzag wrinkles. The collapsed region assumes Bernal stacking configurations AB_1' or AB_2'[38], as illustrated in Fig. 1c, in which one of the graphene sublattices couples to itself upon folding since the two layers are mirror-symmetric with respect to each other. Such a coupling breaks the sublattice symmetry and hence the electron-hole symmetry[39,40].

Secondly, ballistic transmission $T(E, k_{//})$ shows pronounced oscillations over broad energy ranges. Apart from making transmission highly energy-dependent, such oscillations also affect average conductance at a finite bias. The oscillations are clearly visible in the side panels of Fig. 2a–d that show transmission at a fixed momentum $k_{//} = 2\pi/(3a_0)$ that corresponds to the projections of the Dirac points. Further analysis shows that the energy separation Δ_E between the peaks has an approximately linear dependence on Δ_W (Fig. 2e). Such a dependence is the signature of the interference between the interlayer and intralayer transport channels, as found by some of us previously in the case of the electromechanical response of bilayer graphene[14]. The underlying mechanism is further addressed in Section. We would also like to point out that similar transport phenomena dominated by interlayer tunneling have also been observed in break-junction systems[41,42].

The second family of investigated commensurate configurations is defined by $\mathbf{v} = (1, 1)$, that is wrinkles are oriented along the armchair direction. Atomic relaxation effects are more complex in such wrinkles. Unlike in the zigzag case, realizing the lowest-energy Bernal stacking is possible only at a cost of introducing a shear deformation as shown in Fig. 3a. Consequently, the Bernal stacking is not achieved at small values of Δ_W, and the collapsed region assumes the saddle-point (SP) stacking configuration[43] that does not break sublattice symmetry. Figure 3b presents the evolution of shear deformation Δ_y upon the change of Δ_W with $\Delta_y = a_0/(2\sqrt{3})$ representing the pure Bernal stacking configuration. Figure 3c–d present the transmission maps for the armchair wrinkles with $\Delta_W = 40$ Å and $\Delta_W = 120$ Å. In the case of $\mathbf{v} = (1, 1)$,

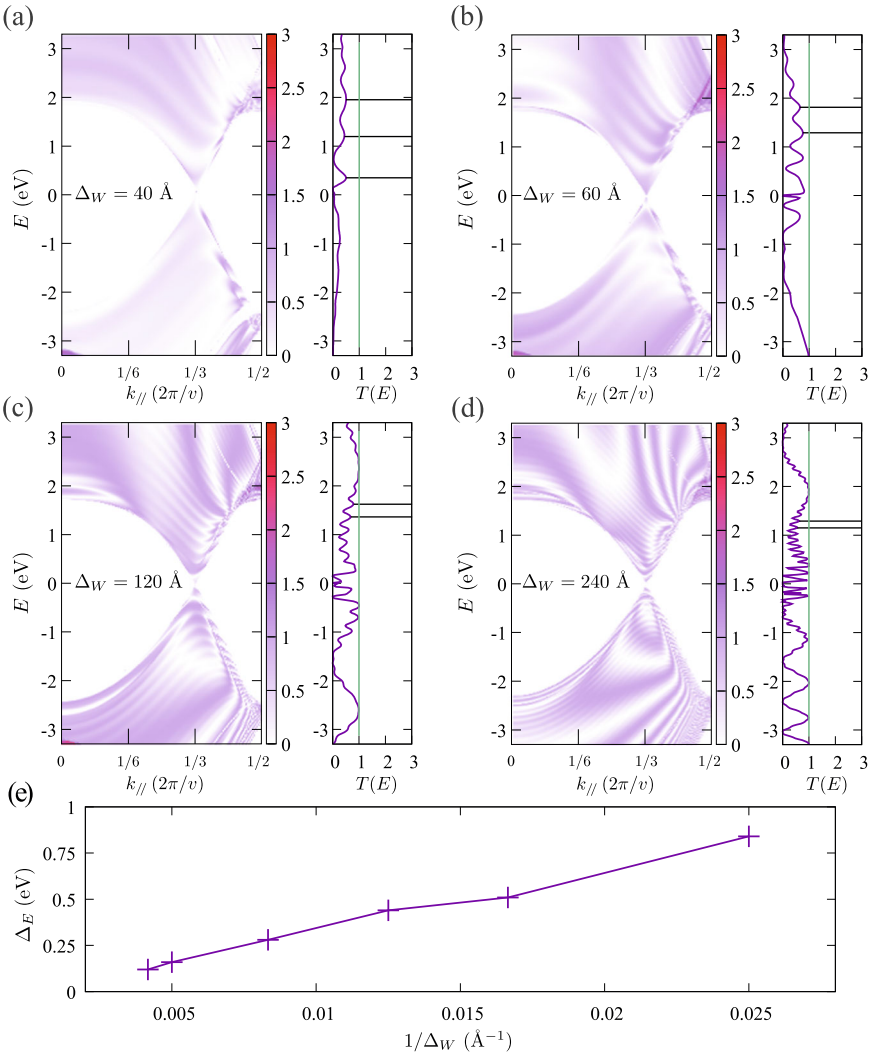

Fig. 2 Electronic transport across commensurate zigzag wrinkles. Ballistic transmissions $T(E, k_{//})$ across zigzag wrinkle models characterized by **a** $\Delta_W = 40$ Å, **b** $\Delta_W = 60$ Å, **c** $\Delta_W = 120$ Å and **d** $\Delta_W = 240$ Å calculated from first principles. The side panels show the transmission probability at $k_{//} = 2\pi/(3a_0)$ which corresponds to the projections of the Dirac points. The energy spacing Δ_E between the oscillation peaks are highlighted by lines. Vertical lines indicate the quantized transmission in the absence of scattering. **e** Dependence of Δ_E on $1/\Delta_W$.

the Dirac points are projected onto $k_{//} = 0$. Similar to the case of zigzag wrinkles, oscillations with the $\Delta_E \propto 1/\Delta_W$ period are observed in the transmission maps. The oscillation pattern is more regular than in the case of $\Delta_W = 40$ Å armchair wrinkle, which assumes the SP stacking and hence preserves electron-hole symmetry. In contrast, the $\Delta_W = 120$ Å wrinkle is significantly closer to the Bernal stacking (see Fig. 3b) and the electron-hole symmetry appears to be well visible in this case.

Conductance oscillations in the atomic chain model

In order to further address the physical mechanism underlying the conductance oscillations observed in both the zigzag and armchair wrinkles, we introduce a simple one-dimensional model treated using the tight-binding approximation. The presence of interlayer conductance channels is defined by Δ_W, and also l that represents the absence of interlayer hopping in the loop-like region as shown in Fig. 4a. At the same time, we observe that $k_{//}$ does not have any significant effect on the oscillation period, hence we introduce a one-dimensional chain described using the nearest-neighbor tight-binding model with an extra hopping t' that models interlayer coupling in graphene wrinkles. Schematic diagram of this model with hopping t' represented by a rainbow-like graph is shown in Fig. 4b. The ratio of the newly introduced hopping t' to the nearest-neighbor hopping t is chosen to resemble that of graphene wrinkles $t'/t = 0.48$ eV/-2.7 eV[7,33]. Figure 4c shows transmission T as a function of energy E at a fixed Δ_W=12 in units of intersite distance, while parameter l is varied. We observe that oscillation peaks have the same positions, which indicates that l is of little effect on the oscillation period. Combined with the results of DFT calculations we conclude that the oscillations are defined by the largest path difference Δ_W. We further analyze the transmission oscillations in the atomic chain model using the non-equilibrium Green's functions (NEGF) approach, in which hoppings t' are treated as a perturbative correction to the transmission.

First, we define an infinite atomic chain with the Hamiltonian

$$H = t \sum_i c_i^\dagger c_{i+1} + h.c., \tag{1}$$

where $c_i(c_i^\dagger)$ is the annihilation (creation) operator on the ith site. This Hamiltonian commutes with the translation operator, thus the energy eigenstates are also momentum eigenstates.

In the NEGF formalism[44,45], the transmission is calculated as

$$T(E) = \mathrm{Tr}[\Gamma_1 G \Gamma_2 G], \tag{2}$$

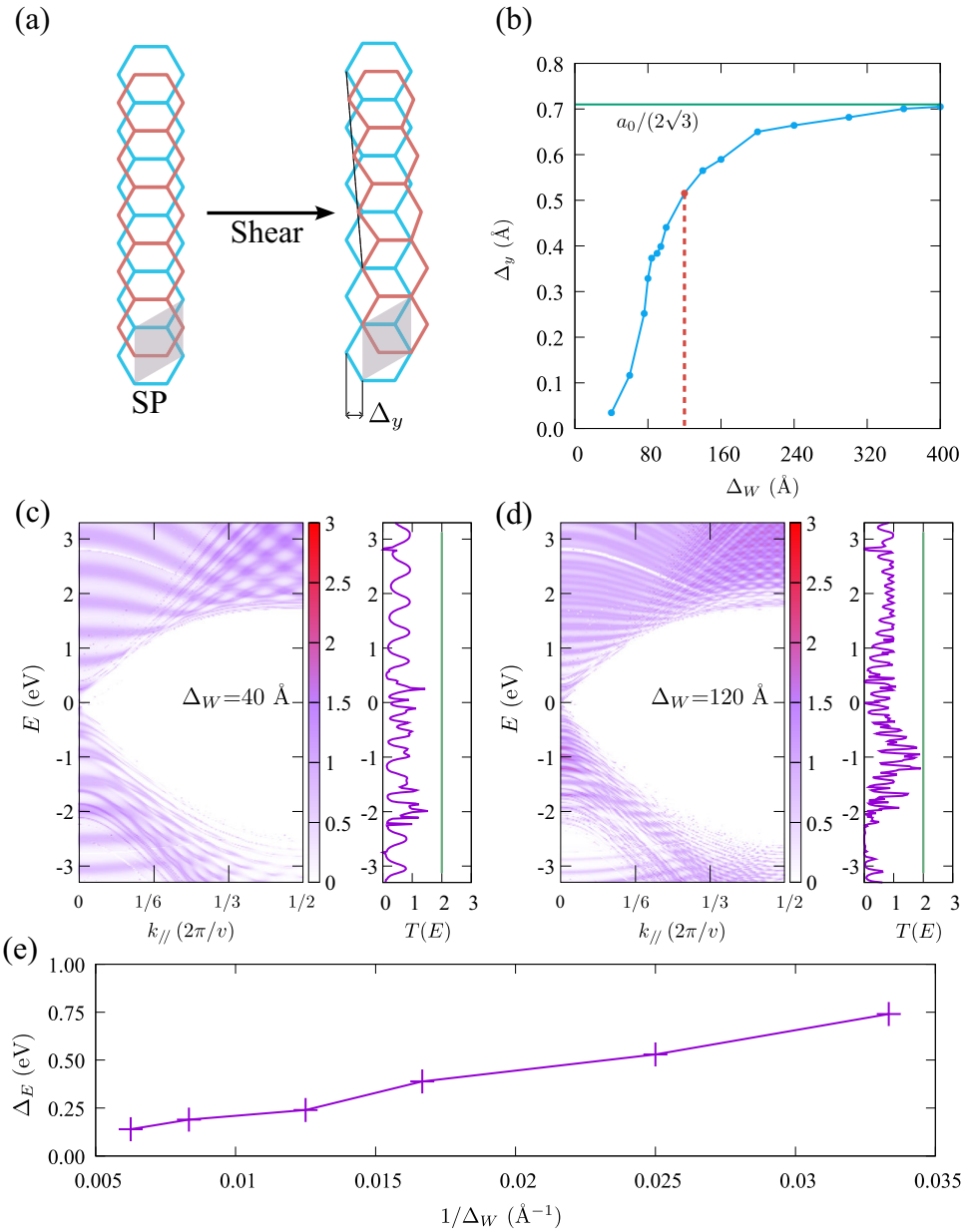

Fig. 3 Electronic transport across commensurate armchair wrinkles. a Schematic illustration of the shear deformation in armchair wrinkles. The shear is characterized by displacement Δ_y. **b** Evolution of shear deformation Δ_y versus compressive displacement Δ_W. At small values of Δ_W, shear deformation Δ_y is small, which corresponds to to the SP stacking configuration ($\Delta_y = a_0/(2\sqrt{3})$ corresponds to pure Bernal stacking. Ballistic transmissions $T(E, k_{//})$ across armchair wrinkle models defined by **c** $\Delta_W = 40$ Å and **d** $\Delta_W = 120$ Å. The $T(E)$ cross sections are taken at $k_{//} = 0$ that corresponding to the projected Dirac points. Vertical lines indicate the quantized transmission in absence of scattering. **e** Dependence of Δ_E on $1/\Delta_W$.

where G is the Green's function $G(E)=[E-H-\Sigma]^{-1}$. The coupling matrices Γ_i are given by $\Gamma_i=i(\Sigma_i-\Sigma_i^\dagger)$, with Σ_i being the self-energies of the two semi-infinite leads.

Green's function G_0 describes the chain in absence of t', while adding coupling t' that models interlayer coupling in wrinkles adds an additional term

$$\Delta h = t' \sum_{i=l/2}^{\Delta_W/2} c_i^\dagger c_{-i} + h.c. \tag{3}$$

The Green's function is then

$$\begin{aligned} G(E) &= \tfrac{1}{G_0^{-1}-\Delta h} \\ &= G_0 + G_0 \Delta h G_0 + G_0 (\Delta h G_0)^2 + \dots . \end{aligned} \tag{4}$$

Keeping only the first order of correction $G_0 \Delta h G_0$, the transmission becomes

$$\begin{aligned} T &= \mathrm{Tr}[\Gamma_1 G_0 \Gamma_2 G_0 \\ &\quad + \Gamma_1 G_0 \Gamma_2 (G_0 + G_0 \Delta h G_0) \\ &\quad + \Gamma_1 (G_0 + G_0 \Delta h G_0) \Gamma_2 G_0 \\ &\quad + \Gamma_1 (G_0 + G_0 \Delta h G_0) \Gamma_2 (G_0 + G_0 \Delta h G_0)]. \end{aligned} \tag{5}$$

The Green's function can be written as an expansion involving eigenstates $|\psi_n\rangle$ of the chain with no hoppings t'

$$G_0(E) = \sum_n \frac{1}{E + \varepsilon i - E_n} |\psi_n\rangle\langle\psi_n|, \tag{6}$$

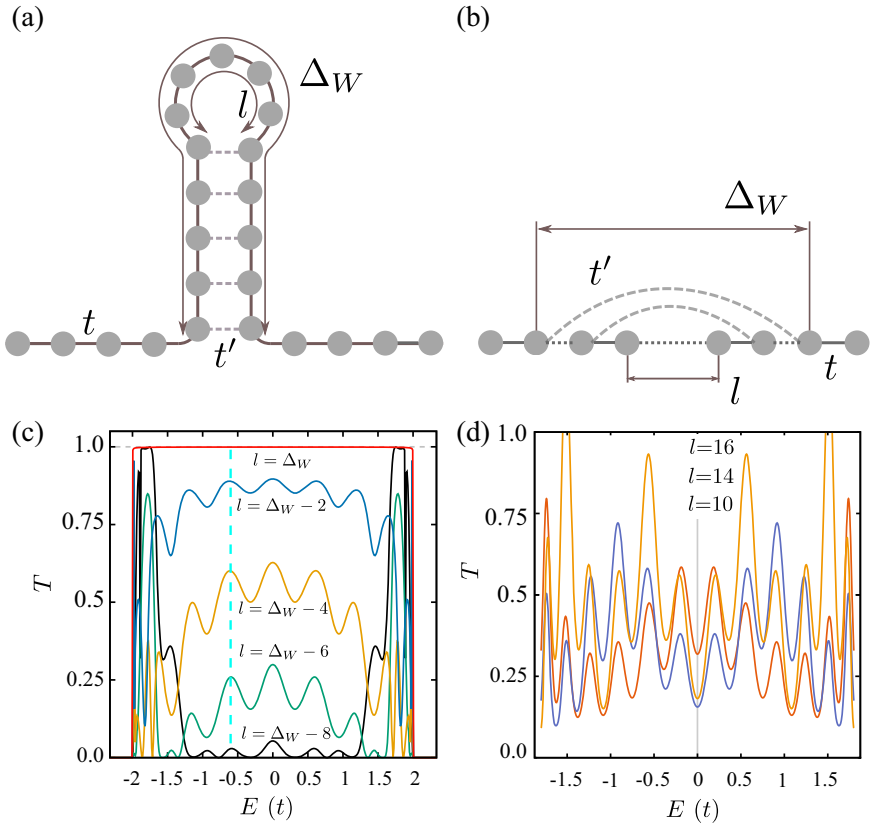

Fig. 4 Transmission oscillations in the atomic chain model. a Cross-section drawing of the trivialized graphene wrinkle and **b** its unfolded representation equivalent to atomic chain with additional hoppings t'. **c** Transmission T as a function energy E in units of t calculated using the TB model Hamiltonian. In this plot, $\Delta_W = 12$ in units of intersite distance is fixed, while different curves correspond to difference values of l. **d** First-order correction to the Green's function $\delta(E) = G_0 \Delta h G_0 / G_0$ plotted for different l and constant $\Delta_W = 20$ reveals that the period of oscillations is governed by Δ_W.

and the correction term $G_0 \Delta h G_0$ becomes

$$G_0 \Delta h G_0 = \sum_m \sum_n \frac{|\psi_m\rangle\langle\psi_m|\Delta h|\psi_n\rangle\langle\psi_n|}{(E + \varepsilon i - E_m)(E + \varepsilon i - E_n)}. \tag{7}$$

As the simplest case, we analyze the $E_n = E_m$ correction $G_0 \Delta h G_0 = \langle\psi_n|\Delta h|\psi_m\rangle G_0$ that gives an E_i-dependent prefactor to the Green's function. We write the factor as a function $\delta(E)$ as

$$\delta(E) G_0 = G_0 \Delta h G_0. \tag{8}$$

The leading order of transmission correction is $\Gamma_1(G_0 + G_0 \Delta h G_0)$ $\Gamma_2(G_0 + G_0 \Delta h G_0)]$, hence the correction to transmission contains $\delta^2 + 4\delta + 1$.

We then evaluate the correction $\delta(E)$, keeping in mind that the eigenstates of the pristine chain

$$\hat{H}|\psi(k)\rangle = 2t \cos(k)|\psi(k)\rangle, \tag{9}$$

are also momentum eigenstates. The correction factor δ represents the phase difference between wavefunctions

$$\delta(E) = \sum_i \langle\psi_n(r_i)|\Delta_h|\psi_n(r_{-i})\rangle|_{E_n = E} \tag{10}$$

connected by the additional hoppings t'. It can then be approximated by a sum of sinusoidal functions

$$\delta(k) = \frac{t'}{t} \sum_{i=l/2}^{\Delta_W/2} \cos(2ik). \tag{11}$$

The results of the summation shown in Fig. 4d suggests that the highest-frequency component in Eq. (11), which corresponds to the interference path Δ_W, defines the oscillation peaks. Our first-principles results are consistent with the conclusions of this simple model.

Transport across incommensurate wrinkles

We will now discuss graphene wrinkles formed along general crystallographic directions $\mathbf{v} = (a, b)$ other than high-symmetry zigzag and armchair orientations. In these cases, the collapsed region locally forms twisted bilayer graphene with matching vectors (a, b) and (b, a). The resulting twist angle is

$$\theta = \arccos\left(\frac{a^2 + 4ab + b^2}{2(a^2 + ab + b^2)}\right), \tag{12}$$

while the translational vector along the wrinkle has a length of $d = \sqrt{a^2 + b^2 + ab}$.

We discuss the effect of wrinkle direction (a, b) on the transmission $T(E, k_{//})$. Translational vector (a, b) defines a one-dimensional mini Brillouin zone (mBZ) obtained by projecting the 2D Brillouin zone of graphene onto the $k_{//}$ direction in momentum space. The Dirac cones of graphene are projected onto either $k_{//} = 0$ (class Ia) or $k_{//} = 2\pi/(3|\mathbf{v}|)$ (class Ib) of the mBZ according to the classification introduced in ref. [46]. Class Ia is defined by $|a - b| \bmod 3 = 0$, class Ib otherwise. The projections of the Dirac cones define the regions in the $T(E, k_{//})$ maps where transmission is allowed and limited by n conductance channels in case of n-fold degeneracy of bands at given E and $k_{//}$ in the ballistic regime.

The periodic structure of wrinkles results in consequences deeper than just the conservation of momentum $k_{//}$ upon ballistic transmission. We stress that semi-infinite graphene sheets on both

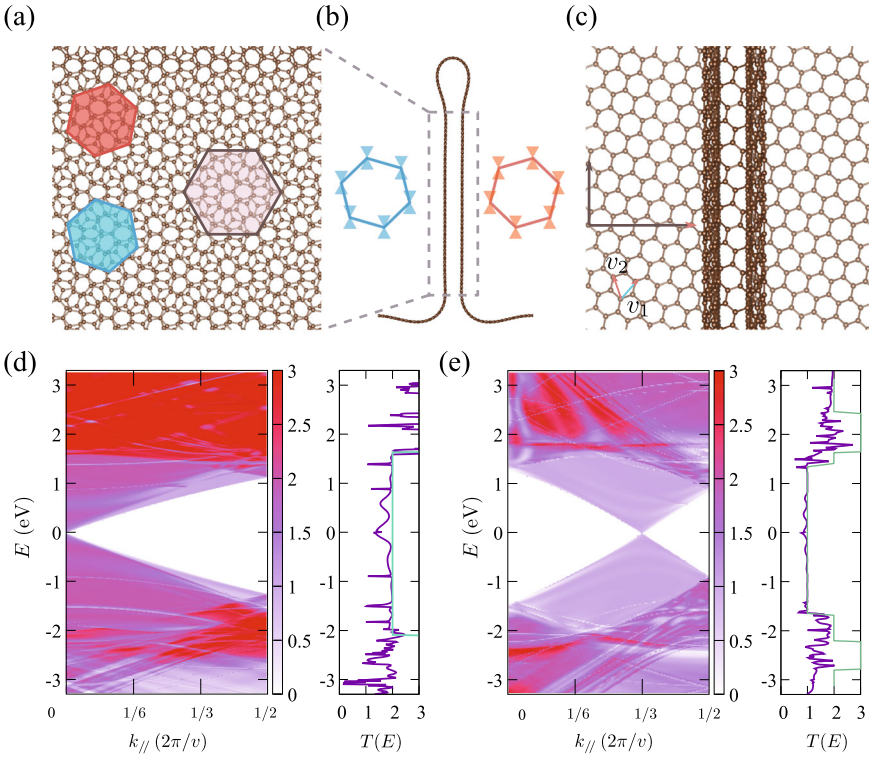

Fig. 5 Electronic transport across incommensurate wrinkles. Atomic structure of incommensurate wrinkle defined by the (1,2) direction: **a** local structure of the collapsed region equivalent to twisted bilayer graphene (unit cell is shown with the shaded region), **b** side-view with the sketch of the Brillouin zones and the Dirac cones of adjacent layers, and **c** top-view of the wrinkle illustrating the conservation of crystallographic orientation of graphene leads. Transmission maps $T(E, k_{//})$ across wrinkle models defined by **d** $\mathbf{v} = (1, 4)$ and $\Delta_W = 80$ Å (class Ia), **e** $\mathbf{v} = (1, 2)$ and $\Delta_W = 80$ Å (class Ib). Vertical lines indicate the quantized transmission in the absence of scattering.

sides of wrinkles of constant width have the same crystallographic orientation. The momentum conservation implies suppressed backscattering at the Dirac point, which can be observed by evaluating contribution to the transmission from the first-order correction $G_0\Delta h G_0$. Starting with the pristine graphene and a simple interlayer containing only hopping between aligned atoms

$$\Delta h_{ij} = \begin{cases} t', & r_i^{\perp} = r_j^{\perp} \\ 0, & r_i^{\perp} \neq r_j^{\perp}, \end{cases} \tag{13}$$

the effective ΔG writes

$$G_0\Delta h G_0(z) = \sum_m \sum_n \frac{\langle\psi_m|\Delta h|\psi_n\rangle}{(z - E_m)(z - E_n)} |\psi_m\rangle\langle\psi_n|, \tag{14}$$

which becomes most significant at $E_m = E_n = z$. Recalling the fact that $|\psi_m\rangle$ and $|\psi_n\rangle$ are eigenstates of pristine graphene, $\langle\psi_m|\Delta h|\psi_n\rangle$ gives an $\exp(2\pi i(\mathbf{k}_m - \mathbf{k}_n)\cdot\mathbf{r}_{ij})$ term. Integrating over $\mathbf{r}_{ij}$, ΔG vanishes if $\mathbf{k}_m \neq \mathbf{k}_n$, while the wrinkle enforces a transformation $\mathbf{k}_m = \mathcal{M}_x\mathbf{k}_n$ due to its mirror-symmetric stacking configuration of the two layers as shown in Fig. 5a–c. Here, $\mathcal{M}_x$ denotes the mirror-reflection with respect to transport direction x: $\mathcal{M}_x(k_x, k_y) = (-k_x, k_y)$. From the above rules of momentum conservation, we conclude that the transmission is only affected in the overlapping region of the Dirac cones. In the non-overlapping region, the correction $G_0\Delta h G_0$ is vanishing, and the transmission retains the value of ideal, defect-free graphene. These results are verified by the explicit DFT transport calculations as shown in Fig. 5d–e for class Ia and class Ib wrinkles, respectively. The transmission maps $T(E, k_{//})$ have overall shape of the Dirac cone projections. Transmission values near the charge neutrality are $T\approx2$ and $T\approx1$ for class Ia and Ib configurations, respectively, indicating that interlayer tunnelling plays a minor role. At higher energies where the Dirac cones overlap, e.g. near $E\approx2$ eV in Fig. 5e, backscattering becomes significant leading to a series of transmission dips. We also point out that class Ia presents larger backscattering from the interlayer coupling since the projected Dirac cones overlap with each other.

Transport across graphene folds

We will now discuss folds as the ultimate regime of out-of-plane disorder in graphene. Folds realize triple-layer graphene configurations in their collapsed regions (Fig. 6a–c). Importantly, adjacent layers (pairs 1–2 and 2–3) in incommensurate folds are twisted with respect to each other, while the outside layers 1 and 3 are aligned. This configuration is equivalent to mirror-symmetric twisted trilayer graphene. While we still expect the effect of interlayer coupling to be weakened by the incommensuration, our DFT calculations predict a larger degree of backscattering in folds than in wrinkles (compare Figs. 5e and 6d for the (1,2) direction). For the folded region of width $l_f = 40$ Å, the average transmission in the energy interval (−0.15 eV, 0.15 eV) is 0.727, while in the wrinkle of equivalent $\Delta_W = 80$ Å it is 0.908. The observed transport behaviour raises the question of whether the enhanced backscattering in incommensurate folds as compared to wrinkles originates from the direct coupling of the outmost layers 1 and 3. The corresponding matrix elements of the Hamiltonian in localized-basis-set first-principles calculations[35,47], are found to be negligible. The estimated Slater-Koster coupling also has a negligible magnitude of 10^{-4} eV. Therefore, we attribute the enhanced scattering to the fact that the number of interlayer tunneling channels is doubled in the folds. As expected, for a commensurate zigzag fold (Fig. 6d) we observe strong

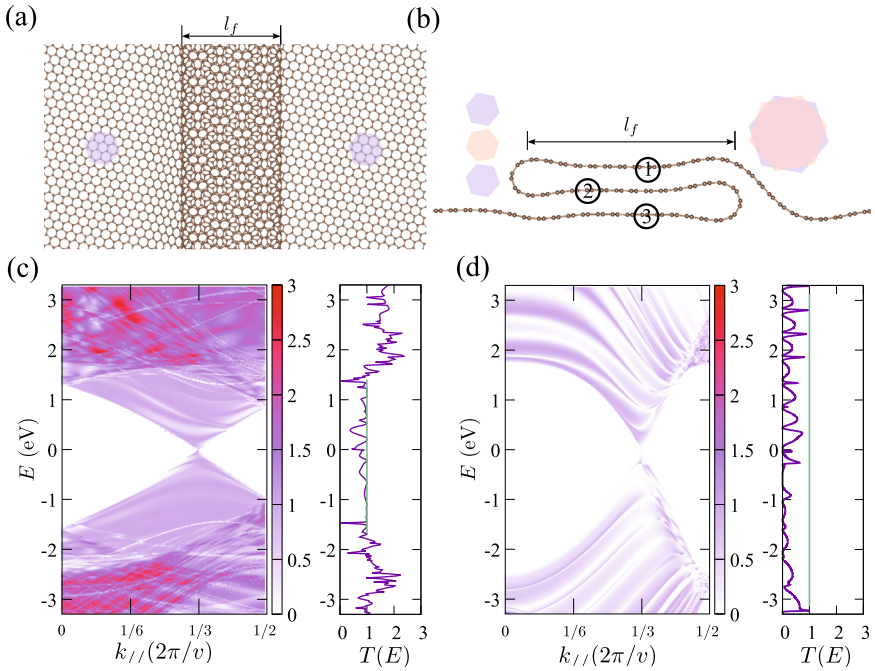

Fig. 6 Electronic transport across graphene folds. a Atomic structure of an incommensurate fold defined by **v** = (1,2) as an example. **b** Side-view of the fold with layers numbered and Brillouin zone orientations indicated. Transmission maps $T(E, k_{//})$ for **c** the incommensurate fold shown in the above panels and **d** zigzag fold characterized by $\Delta_W = 80$ Å. Vertical lines indicate the quantized transmission in absence of scattering.

backscattering with transmission magnitudes lower than in the equivalent zigzag wrinkles (Fig. 2).

DISCUSSION

We investigated the effect of out-of-plane disorder on the electronic transmission in graphene. Different forms of out-of-plane disorder exist in graphene, depending on the compressive displacement and the orientation of the deformation. Our work addressed ballistic transmission through the wrinkles and folds using first-principle calculations, taking into account their width and interlayer commensuration.

The interlayer coupling was found to cause substantial oscillations in the electronic transmission across commensurate wrinkles. Such oscillations were found to originate from the quantum interference involving the interlayer tunneling channels. Based on DFT calculations, we propose a simple one-dimensional model that fully captures the observed oscillations. On the other hand, in incommensurate, "twisted" wrinkles the interlayer coupling is effectively weaker, and the transmission near the Fermi level preserves that of pristine, flat graphene. We have also found enhanced backscattering in folds that was attributed to the doubled contact region in this type of out-of-plane disorder.

Even though our work focuses on understanding physical mechanisms underlying a single event of ballistic transmission across out-of-plane defects in graphene, these results can be translated to mesoscopic properties resulting from multiple scattering events, e.g. electronic transport in diffusive and localization regimes. This allows to apply use the results of our work to samples and devices of diverse morphologies of the out-of-plane disorder. Furthermore, same knowledge can be used for breeding ideas of novel devices based on new operating regimes, e.g. exploiting the combination of the discussed interference phenomena and electromechanical coupling. One example of such a electromechanical phenomenon was discussed by us previously[14], and we believe our work will stimulate further efforts in this direction.

As a generalization, the principles presented in our work are expected to apply also to other types of 2D materials. Formation of locally twisted bilayers in the wrinkles and folds provides an interesting outlook for further studies, e.g. of "twisted" wrinkles in the smaller-angle regime. Even though explicitly addressing the small-angle regime is challenging for standard DFT calculations, we can still anticipate transport properties at small angles. One important aspect is the presence of significant lattice relaxation in bilayer graphene at small twist angles[33]. This relaxation drives incommensurate stacking into the lattice of Bernal stacked AB and BA domains, and hence the emergence of scattering associated with commensurate configurations discussed in our work. Another important aspect is the development of band gaps between the flat-band manifold and remote bands, which is another consequence of lattice relaxation, and the emergence of correlated insulator states at low temperatures at the magic angle and at specific charge-carrier densities[48]. Both effects would contribute to the development of transport gaps. We anticipate that transmission across wrinkles and folds characterized by small twists inherits transport properties of both commensurate and incommensurate configurations.

METHODS

Structure relaxation with classical force fields

The atomic structures of models of the out-of-plane disorder in graphene were obtained by means of the classical force field simulations using LAMMPS[49,50]. The classical force field includes the bond-order potential for describing covalent bonding[51] as well as the modified version of the Kolmogorov-Crespi registry-dependent potential[52] for describing the interlayer van der Waals interactions. The energy minimization was performed using the conjugate-gradient and fire algorithms.

The tight-binding model calculations

In order to describe both the interlayer coupling and the effect of curvature in the tight-binding calculations of graphene with out-of-plane disorder, we employ the Slater-Koster model[7,37]. The p_z atomic orbitals of carbon atoms form the intralayer π bonds and the interlayer σ bonds. The general form of the Hamiltonian including both contributions is

$$\hat{H} = \sum_{i,j} t_{\pi}^{ij} c_i^{\dagger} c_j + \sum_{i,j} t_{\sigma}^{ij} c_i^{\dagger} c_j. \tag{15}$$

Explicit expressions for the hoppings t_{π}^{ij} and t_{σ}^{ij} are[7]

$$t_{\pi}^{ij} = V_{\pi}^{0} \exp\left(-\frac{r - a_0}{r_0}\right) |\sin\theta_i \sin\theta_j|, \tag{16}$$

$$t_{\sigma}^{ij} = V_{\sigma}^{0} \exp\left(-\frac{r - d_0}{r_0}\right) |\cos\theta_i \cos\theta_j|. \tag{17}$$

Following the previous[7] Slater-Koster parametrization, we set $V_{\pi}^{0} = -2.7$ eV, $V_{\sigma}^{0} = 0.48$ eV, characteristic distances $a_0 = 1.42$ Å, $d_0 = 3.35$ Å and the decay length $r_0 = 0.184a$ ($a = \sqrt{3}a_0 = 2.46$ Å as defined in the main text). In the orientation-dependent terms, angles θ_i and θ_j are defined as the angle between $\mathbf{r}_{ij}$ and the local normal vector at atomic positions $\mathbf{r}_i$ and $\mathbf{r}_j$, that is $\theta_i = \angle(\mathbf{r}_{ij}, \mathbf{n}_i)$. These terms accounts for the effect that the local curvature of graphene sheet on the overlap between p_z orbitals.

Recursive Green's function methods

The ballistic transmission was calculated using the non-equilibrium Green's function methods in both the TB model and DFT calculations. The transmission probability is expressed as

$$T_{ij}(E) = \mathrm{Tr}[\Gamma_i G \Gamma_j G], \tag{18}$$

where G is the Green's function $G = [G_0 - \Sigma]^{-1}$. The Γ matrices contains the self-energy terms of the two leads

$$\Gamma_i(E) = i[\Sigma_i(E) - \Sigma_i^{\dagger}(E)]. \tag{19}$$

The self-energy from the ith lead is calculated as $\Sigma_i = h_i G_i h_i^{\dagger}$, where h_i is the coupling matrix between the lead and the scattering region. For each of the semi-infinite leads, Green's function G_i is obtained through the recursive Green's function methods. In each step one layer is added to the lead, and the Green's function iterates as $g_j = [E - h - T g_{j-1} T^{\dagger}]^{-1}$. G_i is taken as the converged value of g, that is $G_i = g_j^{j \to \infty}$.

First-principles electronic transport calculations

First-principles transport calculations were performed with TranSIESTA package[35,36]. We used the double-ζ plus polarization basis set combined with the local density approximation exchange-correlation functional[53]. The energy shift for constructing the localized basis was set to 275 meV, and the real-space cutoff to 250 Ry. The estimation of the direct coupling between the top and bottom layers in graphene folds was extracted from the localized basis set Hamiltonian using the sisl package[47].

DATA AVAILABILITY

The data that support the findings of this study can be obtained from the authors upon reasonable request.

CODE AVAILABILITY

The structural optimization and DFT calculations were performed using the publicly accessible codes LAMMPS and TranSIESTA. The routines for generating the wrinkle configurations and for performing the electronic transport calculations within the tight-binding approximation can be obtained from the authors upon reasonable request.

Received: 21 May 2023; Accepted: 1 December 2023;
Published online: 05 January 2024

REFERENCES

1. Castro Neto, A. H., Guinea, F., Peres, N. M. R., Novoselov, K. S. & Geim, A. K. The electronic properties of graphene. *Rev. Mod. Phys.* **81**, 109–162 (2009).
2. Novoselov, K. S. et al. A roadmap for graphene. *Nature* **490**, 192–200 (2012).
3. Deng, B. et al. Wrinkle-Free Single-Crystal Graphene Wafer Grown on Strain-Engineered Substrates. *ACS Nano* **11**, 12337–12345 (2017).
4. Mariani, E. & von Oppen, F. Flexural Phonons in Free-Standing Graphene. *Phys. Rev. Lett.* **100**, 076801 (2008).
5. Croy, A. Bending rigidities and universality of flexural modes in 2D crystals. *J. Phys. Mater.* **3**, 02lt03 (2020).
6. de Lima, A. L. et al. Soliton instability and fold formation in laterally compressed graphene. *Nanotechnology* **26**, 045707 (2015).
7. Zhu, W. et al. Structure and electronic transport in graphene wrinkles. *Nano Lett.* **12**, 3431–3436 (2012).
8. Hattab, H. et al. Interplay of wrinkles, strain, and lattice parameter in graphene on iridium. *Nano Lett.* **12**, 678–682 (2012).
9. Xie, Y., Chen, Y., Wei, X. L. & Zhong, J. Electron transport in folded graphene junctions. *Phys. Rev. B* **86**, 195426 (2012).
10. Pelc, M., Jaskólski, W., Ayuela, A. & Chico, L. Topologically confined states at corrugations of gated bilayer graphene. *Phys. Rev. B* **92**, 085433 (2015).
11. Kang, Y. et al. The role of nanowrinkles in mass transport across graphene-based membranes. *Adv. Funct. Mater.* **30**, 2003159 (2020).
12. Vozmediano, M. A. H., de Juan, F. & Cortijo, A. Gauge fields and curvature in graphene. *J. Phys.: Conf. Ser.* **129**, 012001 (2008).
13. Ortolani, L. et al. Folded graphene membranes: mapping curvature at the nanoscale. *Nano Lett.* **12**, 5207 (2012).
14. Benameur, M. M. et al. Electromechanical oscillations in bilayer graphene. *Nat. Commun.* **6**, 8582 (2015).
15. Guo, Y. & Guo, W. Electronic and field emission properties of wrinkled graphene. *J. Phys. Chem. C* **117**, 692470 (2013).
16. Pereira, V. M., Castro Neto, A. H., Liang, H. Y. & Mahadevan, L. Geometry, mechanics, and electronics of singular structures and wrinkles in graphene. *Phys. Rev. Lett.* **105**, 156603 (2010).
17. Nakajima, H. et al. Imaging of local structures affecting electrical transport properties of large graphene sheets by lock-in thermography. *Sci. Adv.* **5**, eaau3407 (2019).
18. Katsnelson, M. I. & Prokhorova, M. F. Zero-energy states in corrugated bilayer graphene. *Phys. Rev. B* **77**, 205424 (2008).
19. Zhang, J. & Fahrenthold, E. P. Conductance of Buckled N = 5 Armchair graphene nanoribbons. *J. Phys. Chem. Lett.* **11**, 1378 (2020).
20. Deng, S. & Berry, V. Wrinkled, rippled and crumpled graphene: an overview of formation mechanism, electronic properties, and applications. *Materials Today* **19**, 197–212 (2016).
21. Wang, M. et al. Single-crystal, large-area, fold-free monolayer graphene. *Nature* **596**, 519–524 (2021).
22. Pan, Z., Liu, N., Fu, L. & Liu, Z. Wrinkle engineering: a new approach to massive graphene nanoribbon arrays. *J. Am. Chem. Soc.* **133**, 17578–17581 (2011).
23. Lanza, M. et al. Tuning graphene morphology by substrate towards wrinkle-free devices: Experiment and simulation. *J. Appl. Phys.* **113**, 104301 (2013).
24. Liu, N. et al. The origin of wrinkles on transferred graphene. *Nano Res.* **4**, 996–1004 (2011).
25. Hu, H., Xia, K., Zhao, S., Ma, M. & Zheng, Q. Eliminating graphene wrinkles by strain engineering. *Extreme Mech. Lett.* **42**, 101104 (2021).
26. Ma, R.-S. et al. Wrinkle-induced highly conductive channels in graphene on SiO_2/Si substrates. *Nanoscale* **12**, 12038–12045 (2020).
27. Fan, X. et al. Spontaneous folding growth of graphene on h-BN. *Nano Lett.* **21**, 2033–2039 (2021).
28. Rode, J. C. et al. Linking interlayer twist angle to geometrical parameters of self-assembled folded graphene structures. *2D Mater.* **6**, 015021 (2018).
29. Luo, D. et al. Folding and fracture of single-crystal graphene grown on a Cu(111) foil. *Adv. Mater.* **34**, 2110509 (2022).
30. Yang, L.-Z. et al. Origami-controlled strain engineering of tunable flat bands and correlated states in folded graphene. *Phys. Rev. Mater.* **6**, L041001 (2022).
31. Lipson, H. S. & Stokes, A. The structure of graphite. *Proc. R. Soc. A* **181**, 101–105 (1942).
32. Butz, B. et al. Dislocations in bilayer graphene. *Nature* **505**, 533–537 (2014).
33. Gargiulo, F. & Yazyev, O. V. Structural and electronic transformation in low-angle twisted bilayer graphene. *2D Mater.* **5**, 015019 (2017).
34. Ni, M.-Y. & Wakabayashi, K. Stacking sequence dependence of electronic properties in double-layer graphene heterostructures. *Jpn. J. Appl. Phys.* **53**, 06JD03 (2014).

35. Soler, J. M. et al. The SIESTA method for ab initio order-N materials simulation. *J. Phys.: Condens. Matter* **14**, 2745–2779 (2002).
36. Stokbro, K., Taylor, J., Brandbyge, M. & Ordejón, P. TranSIESTA: a spice for molecular electronics. *Ann. N. Y. Acad. Sci.* **1006**, 212–226 (2003).
37. Slater, J. C. & Koster, G. F. Simplified LCAO method for the periodic potential problem. *Phys. Rev.* **94**, 1498–1524 (1954).
38. Gilbert, S. M. et al. Alternative stacking sequences in hexagonal boron nitride. *2D Materials* **6**, 021006 (2019).
39. Sasaki, K.-I., Murakami, S. & Saito, R. Gauge field for edge state in graphene. *J. Phys. Soc. Jpn.* **75**, 074713 (2006).
40. Semenoff, G. W. Chiral symmetry breaking in graphene. *Physica Scripta* **T146**, 014016 (2012).
41. Caneva, S. et al. Mechanically controlled quantum interference in graphene break junctions. *Nat. Nanotechnol.* **13**, 1126–1131 (2018).
42. Tang, Y. et al. Electric field-induced assembly in single-stacking terphenyl junctions. *J. Am. Chem. Soc.* **142**, 19101–19109 (2020).
43. San-Jose, P., Gorbachev, R. V., Geim, A. K., Novoselov, K. S. & Guinea, F. Stacking boundaries and transport in bilayer graphene. *Nano Lett.* **14**, 2052–2057 (2014).
44. Gargiulo, F. & Yazyev, O. V. Topological aspects of charge-carrier transmission across grain boundaries in graphene. *Nano Lett.* **14**, 250–254 (2014).
45. Büttiker, M. Four-terminal phase-coherent conductance. *Phys. Rev. Lett.* **57**, 1761–1764 (1986).
46. Yazyev, O. V. & Louie, S. G. Electronic transport in polycrystalline graphene. *Nat. Mater.* **9**, 806–809 (2010).
47. Papior N., sisl: v 0.12.3, https://zenodo.org/records/8406433.
48. Cao, Y. et al. Correlated insulator behaviour at half-filling in magic-angle graphene superlattices. *Nature* **556**, 80–84 (2018).
49. LAMMPS Molecular dynamics simulator, https://www.lammps.org.
50. Plimpton, S. Fast parallel algorithms for short-range molecular dynamics. *J. Comput. Phys.* **117**, 1–19 (1995).
51. Los, J. H. & Fasolino, A. Intrinsic long-range bond-order potential for carbon: Performance in Monte Carlo simulations of graphitization. *Phys. Rev. B* **68**, 024107 (2003).
52. Kolmogorov, A. N. & Crespi, V. H. Registry-dependent interlayer potential for graphitic systems. *Phys. Rev. B* **71**, 235415 (2005).
53. Perdew, J. P. & Zunger, A. Self-interaction correction to density-functional approximations for many-electron systems. *Phys. Rev. B* **23**, 5048–5079 (1981).

ACKNOWLEDGEMENTS

This work was supported by the Swiss National Science Foundation (grant No. 172543). Computations were performed at the Swiss National Supercomputing Centre (CSCS) under project No. s1146 and the facilities of the Scientific IT and Application Support Center of EPFL.

AUTHOR CONTRIBUTIONS

Y.G. performed calculations, analyzed results and wrote the manuscript. O.V.Y. proposed and supervised the project.

COMPETING INTERESTS

The authors declare no competing interests.

ADDITIONAL INFORMATION

Supplementary information The online version contains supplementary material available at https://doi.org/10.1038/s41699-023-00437-6.

Correspondence and requests for materials should be addressed to Oleg V. Yazyev.

Reprints and permission information is available at http://www.nature.com/reprints

Publisher's note Springer Nature remains neutral with regard to jurisdictional claims in published maps and institutional affiliations.